DTU Library

Bidirectional electrostatic MEMS-tunable VCSELs

Simonsen, Arnhold; Payandeh, Masoud; Hansen, Søren Engelberth; Marchevsky, Andrey; Park, Gyeong Cheol; Sahoo, Hitesh Kumar; Semenova, Elizaveta; Hansen, Ole; Yvind, Kresten

Published in:
Optics Letters

Link to article, DOI:
10.1364/OL.510273

Publication date:
2024

Document Version
Publisher's PDF, also known as Version of record

Citation (APA):
Simonsen, A., Payandeh, M., Hansen, S. E., Marchevsky, A., Park, G. C., Sahoo, H. K., Semenova, E., Hansen, O., & Yvind, K. (2024). Bidirectional electrostatic MEMS-tunable VCSELs. *Optics Letters*, *49*(4), 802-805. https://doi.org/10.1364/OL.510273

Supplemental Document

Optics Letters

Bidirectional electrostatic MEMS-tunable VCSELs: supplement

ARNHOLD SIMONSEN,[1] MASOUD PAYANDEH,[1] SØREN ENGELBERTH HANSEN,[1] ANDREY MARCHEVSKY,[1] GYEONG CHEOL PARK,[2] HITESH KUMAR SAHOO,[1] ELIZAVETA SEMENOVA,[1] OLE HANSEN,[1] AND KRESTEN YVIND[1,*]

[1] *Technical University of Denmark, Anker Engelunds Vej 1, Kongens Lyngby, 2800, Denmark*
[2] *Electronics and Telecommunications Research Institute, 218 Gajeong-ro, Yuseong-gu, Daejeon, Republic of Korea*
[*] *kryv@dtu.dk*

Supplement DOI: https://doi.org/10.6084/m9.figshare.24963945

Parent Article DOI: https://doi.org/10.1364/OL.510273

Bidirectional electrostatic MEMS tunable VCSELs: supplemental information

The detailed derivation of the bidirectional MEMS dynamics as well as the normalized solutions are given in this supplemental document. Also, a derivation of the effective DC spring constant for a grating mirror with stiff suspension is given.

1. DERIVATION OF BIDIRECTIONAL SYSTEM EQUATIONS

A. Bidirectional capacitive actuator

We consider a system comprising two fixed electrodes (top-electrode at $z = z_t$ and potential V_t and bottom-electrode at $z = -z_b$ and potential V_b) with a movable electrode (mass m, spring constant k and potential V_1) at rest position $z = 0$ in-between, see Fig. S1. The electrodes all have

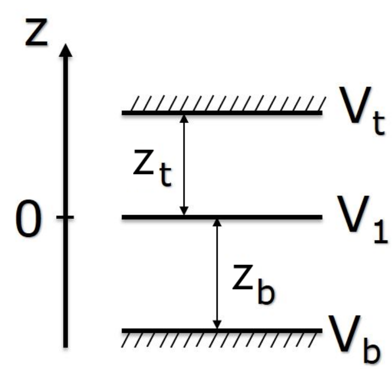

Fig. S1. Two static outer electrodes, one top and one bottom, surround a movable electrode in the middle.

the same area A, and the permittivity of the gap between electrodes is ϵ; thus, the capacitance of the top and bottom capacitors is[1]

$$C_t = C_t(z) = \epsilon A / (z_t - z) \text{ and } C_b = C_b(z) = \epsilon A / (z_b + z), \tag{S1}$$

respectively.

The total Hamiltonian of the system of capacitors, movable electrode and electrical power sources is[2]

$$H(p, z) = \frac{p^2}{2m} + \frac{1}{2}kz^2 + \frac{1}{2}C_t(V_t - V_1)^2 + \frac{1}{2}C_b(V_b - V_1)^2 + \\ + \left[-C_t(V_t - V_1)^2 - C_b(V_b - V_1)^2 + H_{t1} + H_{b1}\right] \tag{S2}$$

where the first term is the kinetic energy (p is the momentum), the second term is the elastic energy stored in the spring, and the next two terms are the energy stored in the capacitors, while the terms in the square bracket are the stored energy in the two electrical power sources that apply the potential differences $V_t - V_1$ and $V_b - V_1$. When the power sources charge up the capacitors, they lose energy as seen in the expression in the square bracket, where H_{t1} and H_{b1} are the initial Hamiltonians of the power sources. In general, when a capacitor C is charged to $Q = CV$ from a constant voltage source, the charge Q flows out of the power source, which therefore looses the energy $\Delta H = -QV = -CV^2$ even though the capacitor only gains $CV^2/2$; the energy difference is lost either as Joule heat in resistive connections or is radiated.

From Hamilton's equations we then have $\partial_t z = \dot{z} = \partial_p H(p, z) = p/m$, or $p = m\dot{z}$ as expected, and $\partial_t p = m\ddot{z} = -\partial_z H(p, z)$ which evaluates to

$$m\ddot{z} = -kz + \frac{1}{2}(V_t - V_1)^2 \frac{\partial C_t}{\partial z} + \frac{1}{2}(V_b - V_1)^2 \frac{\partial C_b}{\partial z} \tag{S3}$$

for a loss-less system.

In Eq. S3 the right-hand side is the restoring force F_{rest}, and for equilibrium the restoring force evaluates to zero, $F_{\text{rest}} = 0$. However, the equilibrium position z_{eq} calculated from the condition $F_{\text{rest}}(z_{\text{eq}}) = 0$ may be stable, metastable, or unstable depending on the sign of $\partial_z F_{\text{rest}}(z) = -k_{\text{eff}}$ where k_{eff} is the effective spring constant in the operating point, i.e., stability requires $k_{\text{eff}} > 0$, while the system is metastable at $k_{\text{eff}} = 0$ and unstable at $k_{\text{eff}} < 0$. From Eq. S3 we get the stability condition

$$k_{\text{eff}} = k - \frac{1}{2}(V_t - V_1)^2 \frac{\partial^2 C_t}{\partial z^2} - \frac{1}{2}(V_b - V_1)^2 \frac{\partial^2 C_b}{\partial z^2} > 0, \tag{S4}$$

which must be combined with the static equilibrium condition $F_{\text{rest}}(z_{\text{eq}}) = 0$, i.e.,

$$-kz_{\text{eq}} + \frac{1}{2}(V_t - V_1)^2 \left.\frac{\partial C_t}{\partial z}\right\rfloor_{z_{\text{eq}}} + \frac{1}{2}(V_b - V_1)^2 \left.\frac{\partial C_b}{\partial z}\right\rfloor_{z_{\text{eq}}} = 0 \tag{S5}$$

to find the range of stable static operating conditions.

Adding dynamic losses (damping $b\dot{z}$) to Eq. S3, carrying out the differentiation and rearranging leads to

$$m\ddot{z} + b\dot{z} + kz = \frac{\epsilon A}{2}\left(\frac{(V_t - V_1)^2}{(z_t - z)^2} - \frac{(V_b - V_1)^2}{(z_b + z)^2}\right), \tag{S6}$$

where the left-hand side represents the pure mechanical equation of motion and the right-hand side the electrostatic actuation.

B. Ideal symmetric actuator

The ideal system is symmetric and has $z_t = z_b = z_0$, and then for $V_1 = 0$ V zero actuation results for $V_t = -V_b = -V_0$ (and also for $V_t = V_b$ which is of no use here). For the perfect symmetric system, we then have

$$m\ddot{z}/z_0 + b\dot{z}/z_0 + kz/z_0 = \frac{\epsilon A V_0^2}{2z_0^3}\left(\frac{(1 + V_1/V_0)^2}{(1 - z/z_0)^2} - \frac{(1 - V_1/V_0)^2}{(1 + z/z_0)^2}\right)$$

with the assumption that $V_t = -V_b = -V_0$. Here the position is normalized to the gap z_0 and actuation voltage V_1 to V_0. The expression can be fully non-dimensionalized as follows

$$\frac{\ddot{z}/z_0}{\omega_0^2} + 2\zeta\frac{\dot{z}/z_0}{\omega_0} + z/z_0 = \frac{\epsilon A V_0^2}{2kz_0^3}\left(\frac{(1 + V_1/V_0)^2}{(1 - z/z_0)^2} - \frac{(1 - V_1/V_0)^2}{(1 + z/z_0)^2}\right) \tag{S7}$$

where $\omega_0 = \sqrt{k/m}$ is the native resonant frequency of the mechanical system alone and $\zeta = b/\left(2\sqrt{km}\right)$ the damping ratio.

Using the same normalization, the stability criterion becomes

$$1 > \frac{\epsilon A V_0^2}{kz_0^3}\left(\frac{(1 + V_1/V_0)^2}{(1 - z/z_0)^3} + \frac{(1 - V_1/V_0)^2}{(1 + z/z_0)^3}\right), \tag{S8}$$

from which it is apparent that with $V_1 = 0$ V, where $z_{\text{eq}} = 0$ the system is only stable for $V_0^2 < kz_0^3/(2\epsilon A) = V_{0\text{PI}_{\text{sym}}}^2$ where $V_{0\text{PI}_{\text{sym}}}$ is the pull-in voltage of the symmetric device at zero actuation voltage V_1. This definition allows for further simplification of the normalized expressions, i.e., the equation of motion

$$\frac{\ddot{z}/z_0}{\omega_0^2} + 2\zeta\frac{\dot{z}/z_0}{\omega_0} + z/z_0 = \frac{V_0^2}{4V_{0\text{PI}_{\text{sym}}}^2}\left(\frac{(1 + V_1/V_0)^2}{(1 - z/z_0)^2} - \frac{(1 - V_1/V_0)^2}{(1 + z/z_0)^2}\right), \tag{S9}$$

and the stability criterion

$$1 > \frac{V_0^2}{2V_{0\text{PI}_{\text{sym}}}^2}\left(\frac{(1 + V_1/V_0)^2}{(1 - z/z_0)^3} + \frac{(1 - V_1/V_0)^2}{(1 + z/z_0)^3}\right). \tag{S10}$$

Defining $u = z/z_0$, $v = V_1/V_0$ and $\Psi^2 = V_0^2/V_{0\text{PI}_{\text{sym}}}^2$ the two equations simplify further to

$$\frac{\ddot{u}}{\omega_0^2} + 2\zeta\frac{\dot{u}}{\omega_0} + u = \frac{1}{4}\Psi^2\left(\frac{(1 + v)^2}{(1 - u)^2} - \frac{(1 - v)^2}{(1 + u)^2}\right), \tag{S11}$$

and

$$1 > \frac{1}{2}\Psi^2\left(\frac{(1+v)^2}{(1-u)^3} + \frac{(1-v)^2}{(1+u)^3}\right), \tag{S12}$$

respectively.

Under static conditions ($\dot{u} = 0$ and $\ddot{u} = 0$), the coefficient Ψ^2 may be eliminated from Eqs. S11 and S12 at pull-in ($k_{\text{eff}} = 0$) to yield

$$2u_{\text{pi}}\left(\frac{(1+v_{\text{pi}})^2}{(1-u_{\text{pi}})^3} + \frac{(1-v_{\text{pi}})^2}{(1+u_{\text{pi}})^3}\right) = \left(\frac{(1+v_{\text{pi}})^2}{(1-u_{\text{pi}})^2} - \frac{(1-v_{\text{pi}})^2}{(1+u_{\text{pi}})^2}\right),$$

where u_{pi} and v_{pi} are normalized deflection and actuation voltage at pull-in, respectively. Rearranging leads to

$$(1+v_{\text{pi}})^2\left(\frac{2u_{\text{pi}}}{(1-u_{\text{pi}})^3} - \frac{1}{(1-u_{\text{pi}})^2}\right) = -(1-v_{\text{pi}})^2\left(\frac{2u_{\text{pi}}}{(1+u_{\text{pi}})^3} + \frac{1}{(1+u_{\text{pi}})^2}\right),$$

and thus

$$\frac{(1-v_{\text{pi}})^2}{(1+v_{\text{pi}})^2} = \frac{-\frac{2u_{\text{pi}}}{(1-u_{\text{pi}})^3} + \frac{1}{(1-u_{\text{pi}})^2}}{\frac{2u_{\text{pi}}}{(1+u_{\text{pi}})^3} + \frac{1}{(1+u_{\text{pi}})^2}} = \frac{(1+u_{\text{pi}})^3}{(1-u_{\text{pi}})^3}\frac{1-3u_{\text{pi}}}{1+3u_{\text{pi}}}.$$

As the left-hand side must be positive, we have $|u_{\text{pi}}| \leq 1/3$, and that $u_{\text{pi}} = \pm 1/3 \Rightarrow v_{\text{pi}} = \pm 1$, while $u_{\text{pi}} = 0 \Rightarrow v_{\text{pi}} = 0$ (if V_0 is non-zero). It follows that

$$\frac{1-v_{\text{pi}}}{1+v_{\text{pi}}} = \pm\frac{\sqrt{(1+u_{\text{pi}})^3\,(1-3u_{\text{pi}})}}{\sqrt{(1-u_{\text{pi}})^3\,(1+3u_{\text{pi}})}},$$

where the positive sign is valid for $|v_{\text{pi}}| \leq 1$.

Solving for the normalized actuation voltage leads to

$$v_{\text{pi}} = \frac{\sqrt{(1-u_{\text{pi}})^3\,(1+3u_{\text{pi}})} \mp \sqrt{(1+u_{\text{pi}})^3\,(1-3u_{\text{pi}})}}{\sqrt{(1-u_{\text{pi}})^3\,(1+3u_{\text{pi}})} \pm \sqrt{(1+u_{\text{pi}})^3\,(1-3u_{\text{pi}})}}, \tag{S13}$$

where the upper sign is valid for $|v_{\text{pi}}| \leq 1$, and the lower sign is valid for $|v_{\text{pi}}| \geq 1$.

Solving the static equilibrium condition (Eq. S11 with $\dot{u} = 0$ and $\ddot{u} = 0$) for Ψ^2 at pull in yields

$$\Psi^2 = \frac{4u_{\text{pi}}}{\frac{(1+v_{\text{pi}})^2}{(1-u_{\text{pi}})^2} - \frac{(1-v_{\text{pi}})^2}{(1+u_{\text{pi}})^2}} = \left(\frac{\sqrt{(1-u_{\text{pi}})^3\,(1+3u_{\text{pi}})} \pm \sqrt{(1+u_{\text{pi}})^3\,(1-3u_{\text{pi}})}}{2}\right)^2 \tag{S14}$$

and thus

$$\Psi = \left|\frac{V_0}{V_{0\text{PI}_{\text{sym}}}}\right| = \left|\frac{\sqrt{(1-u_{\text{pi}})^3\,(1+3u_{\text{pi}})} \pm \sqrt{(1+u_{\text{pi}})^3\,(1-3u_{\text{pi}})}}{2}\right|,$$

in both cases the upper sign is valid for $|v_{\text{pi}}| \leq 1$. We see that at $u_{\text{pi}} = \pm 1/3$ we have $\Psi = \sqrt{4/27}$.

Combining Eqs. S13 and S14 a simple calculation shows that the simple relation $v_{\text{pi}}\Psi^2 = 4u_{\text{pi}}^3$ is valid at pull-in.

C. Real asymmetric, but almost symmetric, actuator

In a real device, it is almost impossible to avoid that $z_t \neq z_b$ such that the system is asymmetric. To account for the asymmetry, we take $z_b = z_0$ and $z_t = \alpha z_0$, where α is the asymmetry factor; moreover we want to work with normalized positions $u = z/z_0$. Likewise we take $V_b = V_0$ and normalize the actuation voltage V_1 to V_0, i.e., $v = V_1/V_0$ while V_t for now remains unassigned. When these assumptions are used in the general equation of motion Eq. S6 we get

$$m\ddot{u} + b\dot{u} + ku = \frac{\epsilon A V_0^2}{2z_0^3}\left(\frac{(V_t/V_0 - v)^2}{(\alpha - u)^2} - \frac{(1-v)^2}{(1+u)^2}\right)$$

and then it becomes apparent that by applying the bias voltage $V_t = -\alpha V_0$ zero actuation at $V_1 = 0$ V results, and with this assignment we get a normalized equation of motion that is quite similar to that for the symmetric actuator

$$\frac{\ddot{u}}{\omega_0^2} + 2\zeta\frac{\dot{u}}{\omega_0} + u = \frac{\epsilon A V_0^2}{2kz_0^3}\left(\frac{(\alpha+v)^2}{(\alpha-u)^2} - \frac{(1-v)^2}{(1+u)^2}\right)$$

and with the corresponding stability criterion

$$\frac{\epsilon A V_0^2}{kz_0^3}\left(\frac{(\alpha+v)^2}{(\alpha-u)^3} + \frac{(1-v)^2}{(1+u)^3}\right) < 1,$$

from which we see that the pull-in voltage at zero actuation voltage ($v = 0$) is $V_{0\mathrm{PI}}^2 = kz_0^3/(\epsilon A\,(1+1/\alpha))$ which leads to the final non-dimensionalized equation of motion

$$\frac{\ddot{u}}{\omega_0^2} + 2\zeta\frac{\dot{u}}{\omega_0} + u = \frac{V_0^2}{2\,(1+1/\alpha)\,V_{0\mathrm{PI}}^2}\left(\frac{(\alpha+v)^2}{(\alpha-u)^2} - \frac{(1-v)^2}{(1+u)^2}\right) = \tag{S15}$$

$$= \frac{1}{2\,(1+1/\alpha)}\Psi_\alpha^2\left(\frac{(\alpha+v)^2}{(\alpha-u)^2} - \frac{(1-v)^2}{(1+u)^2}\right), \tag{S16}$$

with the stability criterion

$$1 > \frac{V_0^2}{(1+1/\alpha)\,V_{0\mathrm{PI}}^2}\left(\frac{(\alpha+v)^2}{(\alpha-u)^3} + \frac{(1-v)^2}{(1+u)^3}\right) = \tag{S17}$$

$$= \frac{1}{(1+1/\alpha)}\Psi_\alpha^2\left(\frac{(\alpha+v)^2}{(\alpha-u)^3} + \frac{(1-v)^2}{(1+u)^3}\right).$$

where $\Psi_\alpha^2 \equiv V_0^2/V_{0\mathrm{PI}}^2$.

Eliminating Ψ_α^2 in static conditions by use of Eqs. S15 and S17 we get

$$2u_{\mathrm{pi}}\left(\frac{(\alpha+v_{\mathrm{pi}})^2}{(\alpha-u_{\mathrm{pi}})^3} + \frac{(1-v_{\mathrm{pi}})^2}{(1+u_{\mathrm{pi}})^3}\right) = \left(\frac{(\alpha+v_{\mathrm{pi}})^2}{(\alpha-u_{\mathrm{pi}})^2} - \frac{(1-v_{\mathrm{pi}})^2}{(1+u_{\mathrm{pi}})^2}\right)$$

which can be rearranged to

$$(\alpha+v_{\mathrm{pi}})^2\left(\frac{2u_{\mathrm{pi}}}{(\alpha-u_{\mathrm{pi}})^3} - \frac{1}{(\alpha-u_{\mathrm{pi}})^2}\right) = -(1-v_{\mathrm{pi}})^2\left(\frac{2u_{\mathrm{pi}}}{(1+u_{\mathrm{pi}})^3} + \frac{1}{(1+u_{\mathrm{pi}})^2}\right)$$

and thus

$$\frac{(1-v_{\mathrm{pi}})^2}{(\alpha+v_{\mathrm{pi}})^2} = \frac{(1+u_{\mathrm{pi}})^3}{(\alpha-u_{\mathrm{pi}})^3}\frac{\alpha-3u_{\mathrm{pi}}}{1+3u_{\mathrm{pi}}}.$$

The left-hand side must be positive, and thus, the normalized pull-in deflection is restricted to the range $-1/3 \le u_{\mathrm{pi}} \le \alpha/3$, and $u_{\mathrm{pi}} = \alpha/3 \Rightarrow v_{\mathrm{pi}} = 1$, $u_{\mathrm{pi}} = -1/3 \Rightarrow v_{\mathrm{pi}} = -\alpha$, and $u_{\mathrm{pi}} = 0 \Rightarrow v_{\mathrm{pi}} = 0$ (as long as V_0 is finite). It follows that

$$\frac{1-v_{\mathrm{pi}}}{\alpha+v_{\mathrm{pi}}} = \pm\frac{\sqrt{(1+u_{\mathrm{pi}})^3\,(\alpha-3u_{\mathrm{pi}})}}{\sqrt{(\alpha-u_{\mathrm{pi}})^3\,(1+3u_{\mathrm{pi}})}}$$

where the positive sign is valid for the range $-\alpha \le v_{\mathrm{pi}} \le 1$, while the negative sign is valid for v_{pi} outside this range. Solving for v_{pi} leads to

$$v_{\mathrm{pi}} = \frac{\sqrt{\left(\alpha - u_{\mathrm{pi}}\right)^3 \left(1 + 3u_{\mathrm{pi}}\right)} \mp \alpha \sqrt{\left(1 + u_{\mathrm{pi}}\right)^3 \left(\alpha - 3u_{\mathrm{pi}}\right)}}{\sqrt{\left(\alpha - u_{\mathrm{pi}}\right)^3 \left(1 + 3u_{\mathrm{pi}}\right)} \pm \sqrt{\left(1 + u_{\mathrm{pi}}\right)^3 \left(\alpha - 3u_{\mathrm{pi}}\right)}}, \tag{S18}$$

where the upper sign is valid in the range $-\alpha \le v_{\mathrm{pi}} \le 1$.

Solving the static equation of motion for Ψ_α^2 leads to

$$\Psi_\alpha^2 = \frac{2\left(1 + 1/\alpha\right) u_{\mathrm{pi}}}{\frac{(\alpha + v_{\mathrm{pi}})^2}{\left(\alpha - u_{\mathrm{pi}}\right)^2} - \frac{(1 - v_{\mathrm{pi}})^2}{\left(1 + u_{\mathrm{pi}}\right)^2}} = \frac{\left(\sqrt{\left(\alpha - u_{\mathrm{pi}}\right)^3 \left(1 + 3u_{\mathrm{pi}}\right)} \pm \sqrt{\left(1 + u_{\mathrm{pi}}\right)^3 \left(\alpha - 3u_{\mathrm{pi}}\right)}\right)^2}{\alpha\left(\alpha + 1\right)^2},$$

and thus

$$\Psi_\alpha = \left|\frac{V_0}{V_{0\mathrm{PI}}}\right| = \frac{\left|\sqrt{\left(\alpha - u_{\mathrm{pi}}\right)^3 \left(1 + 3u_{\mathrm{pi}}\right)} \pm \sqrt{\left(1 + u_{\mathrm{pi}}\right)^3 \left(\alpha - 3u_{\mathrm{pi}}\right)}\right|}{\left(\alpha + 1\right)\sqrt{\alpha}} \tag{S19}$$

where we see that at $u_{\mathrm{pi}} = -1/3$ ($v_{\mathrm{pi}} = -\alpha$) we have $\Psi_\alpha = \sqrt{8/27}/\left(\sqrt{\alpha}\sqrt{1+\alpha}\right)$ while at $u_{\mathrm{pi}} = \alpha/3$ ($v_{\mathrm{pi}} = 1$) we have $\Psi_\alpha = \alpha\sqrt{8/27}/\sqrt{1+\alpha}$.

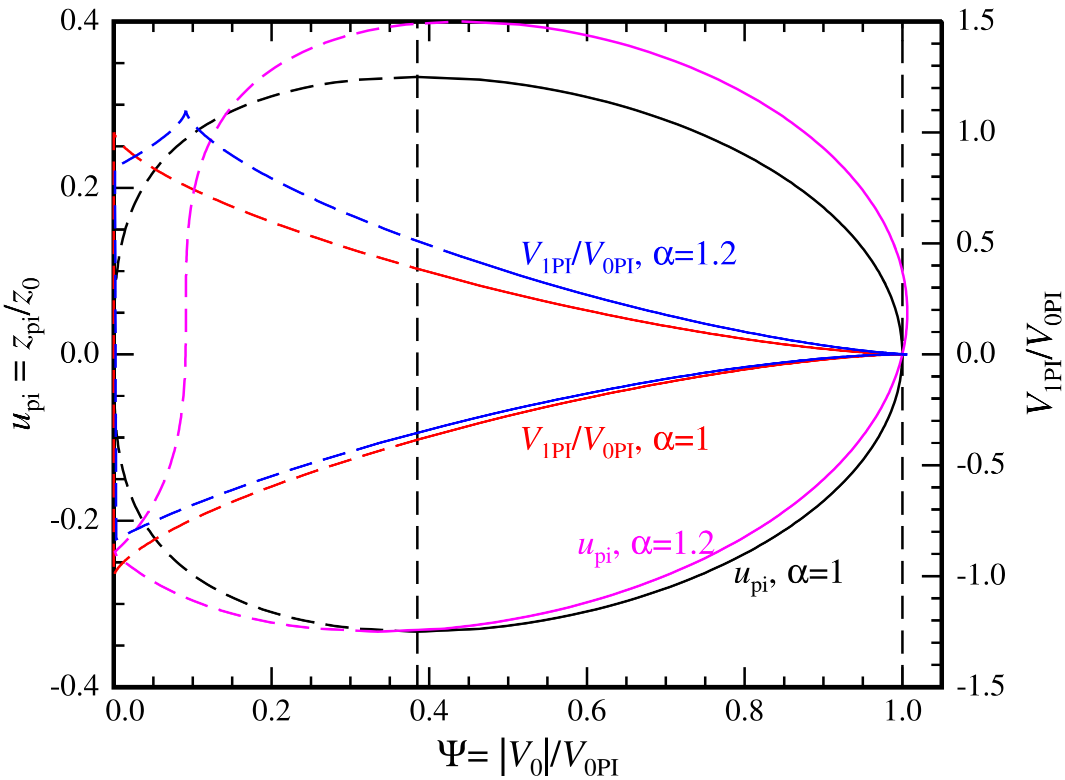

Fig. S2. Normalized pull-in displacement u_{pi} and normalized pull-in voltage $V_{1\mathrm{PI}}/V_{0\mathrm{PI}}$ as a function of normalized bias voltage $\Psi = V_0/V_{0\mathrm{PI}}$ for two values of the asymmetry factor $\alpha = 1$ and $\alpha = 1.2$. The vertical dashed lines indicate $\Psi = \sqrt{4/27}$ and $\Psi = 1$.

Fig. S2 shows calculated normalized pull-in displacement u_{pi} and voltage $V_{1\mathrm{PI}}/V_{0\mathrm{PI}}$ as function of normalized bias voltage $V_0/V_{0\mathrm{PI}}$.

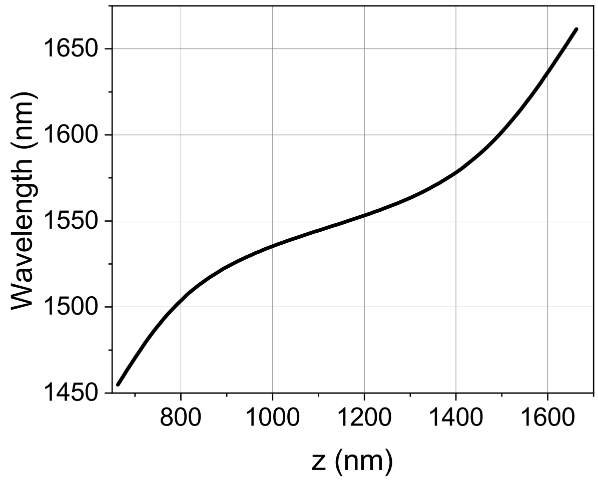

Fig. S3. Wavelength as a function of gap change for the semiconductor coupled MEMS VCSEL.

The peculiar shape of the pull-in displacement curve in Fig. S2 for the asymmetric MEMS near $V_0/V_{0\mathrm{PI}} = 0$ can be understood as follows. The part of the plot which refers to an asymmetric MEMS has $\alpha = 1.2$, i.e., $z_b = z_0$ and $z_t = 1.2z_0$. Starting from the left with $V_0 = 0$ pull-in due to an applied V_1 will happen to the bottom electrode (which is closest) with the normalized pull-in displacement $u_{\mathrm{pi}} = -1/3$, in the same way as for a single parallel-plate MEMS. At $|V_0|/V_{0\mathrm{PI}} \simeq 0.4$ depending on polarity of V_1, pull-in may happen to either the top or the bottom electrodes; if it happens to the top electrode the normalized pull-in displacement becomes $u_{\mathrm{pi}} = z_t/(3z_0) = \alpha/3 = 0.4$ as also seen in Fig. S2. Obviously, if the pull-in displacement is a continuous function of $|V_0|/V_{0\mathrm{PI}}$, the pull-in displacement must be 0 for some specific value of $|V_0|/V_{0\mathrm{PI}}$ on the path from $|V_0|/V_{0\mathrm{PI}} = 0$ to 0.4. A detailed calculation shows that this happens at $|V_0|/V_{0\mathrm{PI}} = (\alpha - 1)/(\alpha + 1) \simeq 0.09$ in the present case, and pull-in happens at $V_1/V_{0\mathrm{PI}} = 2\alpha/(\alpha + 1) \simeq 1.09$ in this case, in agreement with Fig. S2. This deterministic behavior should be compared to the behavior of the symmetric MEMS at $V_0 = 0$, where pull-in due to V_1 happens at random to the top and bottom electrodes. At $|V_0| > 0$ V the pull-in displacement branches to two deterministic curves, one for pull-in to each of the top and bottom electrodes. In the asymmetric case the two pull-in displacement branches are quite dissimilar; on the lower branch pull-in always happens to the bottom electrode, while on the upper branch the pull-in at lower values of $|V_0|$ happens to the bottom electrode and at larger values of $|V_0|$ pull-in happens to the upper electrode.

2. TUNING EFFICIENCY

The bidirectional MEMS VCSEL was simulated using a modal method, as highlighted in[3], and further executed with the assistance of CAMFR[4, 5], as done in [6]. The shape of the curve is typical for "semiconductor coupled cavities"[7] where no AR coating is applied on the gain stack towards the airgap and there is a field maximum at the semiconductor/air interface at the center wavelength (here 1550nm). The detailed material stack is given in [6]. To emulate the tuning effect, alterations were made to the air gap's thickness. With each variation in thickness, the cavity mode was identified; see Fig. S3. The lasing mode was derived by meeting the unity round trip gain condition for the cavity. The design adopted a semiconductor coupling, as prior efforts to integrate an AR coating at the bonding junction were unsuccessful due to issues like roughness or coating stress.

3. EXPERIMENTAL SETUP

Figure S4 provides an illustrative view of the experimental arrangement. The semiconductor laser chip sits on top of a copper chuck, which can be temperature controlled by the connected thermoelectric cooler (TEC). The TEC is on top of an aluminum mount that sits on an XY stage

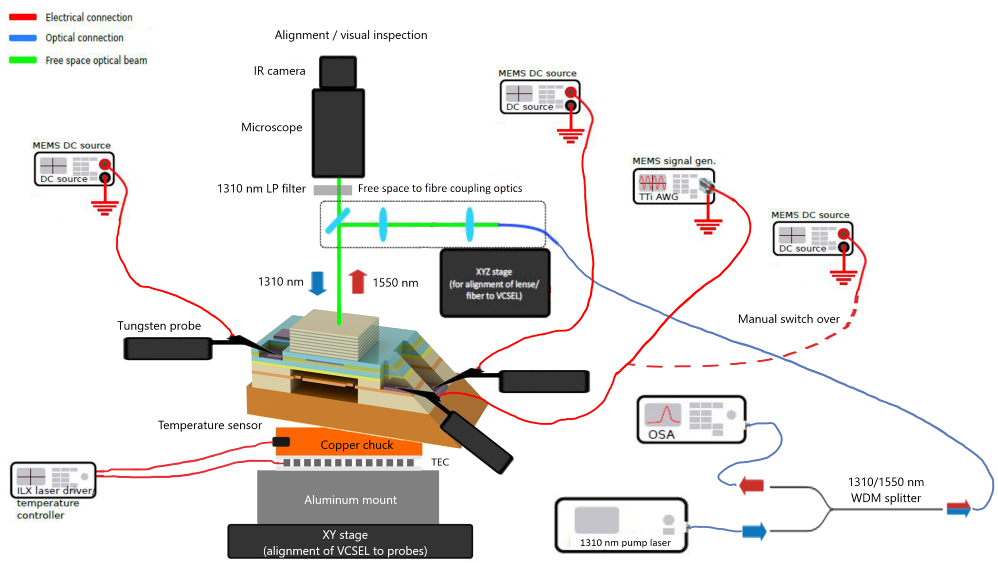

Fig. S4. Experimental probe setup showing spectral characterization of an optically pumped bidirectional MEMS VCSEL.

below a microscope. The setup is referred to as a probe station due to its ability to send electrical signals via probes.

The MEMS VCSEL probe station incorporates three tungsten probes that can be precisely adjusted using micrometer screws along the x, y, and z axes. These probes are connected by BNC cables to two separate MEMS DC power supplies, allowing for the application of direct current voltages to the silicon substrate beneath the lower air gap and to the indium phosphide layer situated above the upper air gap. These DC power supplies are the dual SMU channels from a Keithley 4200-SCS Semiconductor Characterization System[8], which can supply a voltage range of up to ± 210 V. Additionally, an arbitrary waveform generator (AWG) from TTi[9] is linked to the third probe, which interfaces with the silicon-on-insulator (MEMS) layer of the device. In static bidirectional analyses, this AWG is substituted by a third DC source.

A wavelength-stabilized 1310 nm pump laser, from Innolume[10], is fiber coupled to a 1310/1550 nm wavelength division multiplex (WDM) splitter, from Haphit[11], which guides the pump light in the 1310 nm port through the common port and into the microscope. The free space optics consists of a collimating and focusing lens. The incident 1310 nm light is reflected into the microscope's optical path using free space to fibre coupling optics. The 1310 nm light then goes through the dielectric top DBR mirror and gets (partly) absorbed in the multiple quantum wells of the VCSEL. The resulting 1550 nm laser emission exits through the top surface of the wafer, is guided through the same optics as the pump light, and is collimated and focused back into the same fiber. To isolate and remove any reflected pump light, the 1550 nm emission passes through the WDM splitter's common port and is directed to the optical spectrum analyzer (OSA) through the 1550 nm output[12].

To correlate the experimental wavelength findings with the MEMS displacement presented in Fig. 3 (b) of the primary article, the wavelength data is converted to MEMS positional information utilizing Figure S3.

4. BIDIRECTIONAL DYNAMIC EQUATIONS

Assuming an alternating drive signal on the movable electrode, i.e., $V_1(t) = V_a \cos(\omega t)$ where V_a is the amplitude and ω is the actuation frequency, inserted in Eq. (S16) solved for MEMS position

z results in (only including the fundamental sinusoidal term)

$$z(t) = \frac{V_0 V_a}{V_{0PI}^2} \frac{\omega_0^2 z_0 \cos(\omega t - \phi)}{\sqrt{\left(\omega^2 - \omega_0^2\left(1 - \frac{V_0^2}{V_{0PI}^2}\right)\right)^2 + \left(\frac{\omega_0 \omega}{Q}\right)^2}}, \quad \phi = \arctan\left(\frac{\omega_0 \omega}{Q\left(\omega_0^2\left(1 - \frac{V_0^2}{V_{0PI}^2}\right) - \omega^2\right)}\right) \tag{S20}$$

where Q is the mechanical quality factor, ω_0 is the native mechanical resonant frequency. Eq. (S20) resembles the result for the standard unidirectional electrostatic actuator[13] (also only including the fundamental term)

$$z(t) = \frac{4}{27} \frac{2V_0 V_a}{V_{PI}^2} \frac{\omega_0^2 z_0 \cos(\omega t - \phi)}{\sqrt{\left(\omega^2 - \omega_0^2\right)^2 + \left(\frac{\omega_0 \omega}{Q}\right)^2}} + z_{\text{OFST}} \tag{S21}$$

with $V_{PI} = 8z_0^2 k/(27C_0)$, where C_0 is the equilibrium actuator capacitance, and z_{OFST} is an off-set displacement. One difference between the two equations is that the electrostatic spring softening $\sqrt{1 - V_0^2/V_{0PI}^2}$ is seen in the fundamental term for the bidirectional actuator, compared to the first higher-order term for the unidirectional actuator[13].

In both cases, the MEMS displacement amplitude can be increased by increasing the static electric field V_0; however, in the unidirectional case, increasing the DC field increases the offset from the resting mirror position, which will limit the tuning range. For the bidirectional configuration, this offset is not seen, as opposite polarized DC fields of equal magnitude ($\alpha = 1$) will result in electrostatic forces of opposite directions but equal in magnitude, resulting in zero net force on the movable electrode. Therefore, the only cost associated with increasing the DC fields is the reduction of the resonant frequency (electrostatic spring softening). When designing a stiff MEMS, this reduction can be taken into account in order to realize a targeted sweep rate, as seen in Fig.6 in the parent article.

A. Maximum response

For maximum response, a sinusoidal drive signal is used. As previously mentioned, the electrostatic spring softening appears on the fundamental term (assuming a sinusoidal driving signal) for the bidirectional electrostatic actuator. However, for the unidirectional actuator, it appears on the first higher-order term, as a correction to the spring constant, given by[14]

$$K_{elec} = -\frac{\epsilon A V_0^2}{z^3} \tag{S22}$$

which results in the correction to the resonant frequency given by

$$f = \frac{1}{2\pi}\sqrt{\frac{K_0 + K_{elec}}{m}} \tag{S23}$$

where $K_0 = m(2\pi f_0)^2$ is the unaffected spring constant.

The first-order effect of electrostatic spring softening for the bidirectional and unidirectional actuator can be seen in Fig. S5. As indicated, the effect on the adjusted resonant frequency for the bidirectional actuator is significantly higher, for intermediate V_0 values, compared to the onesided actuator. This is because the MEMS is affected by two DC fields in the bidirectional configuration, i.e., from the top and bottom capacitors, while the unidirectional actuator is only affected by one DC field.

The correction of the resonant frequency for the unidirectional actuator shows asymptotic behavior for high static fields since the MEMS is displaced by the applied DC, see Eq. (S22), in contrast to the bidirectional actuator, the MEMS is doubly affected by the applied DC field. In order to take into account ESS for the unidirectional case three for-loops were used, the first loop specifies the DC voltage V_0, the next loop was used to calculate the DC offset with no AC voltage, and subsequently, the resonant frequency given by Eq. (S23) is calculated, and the last loop was used to calculate the maximum displacement given the previously set DC voltage and a set AC voltage, at the adjusted resonance frequency.

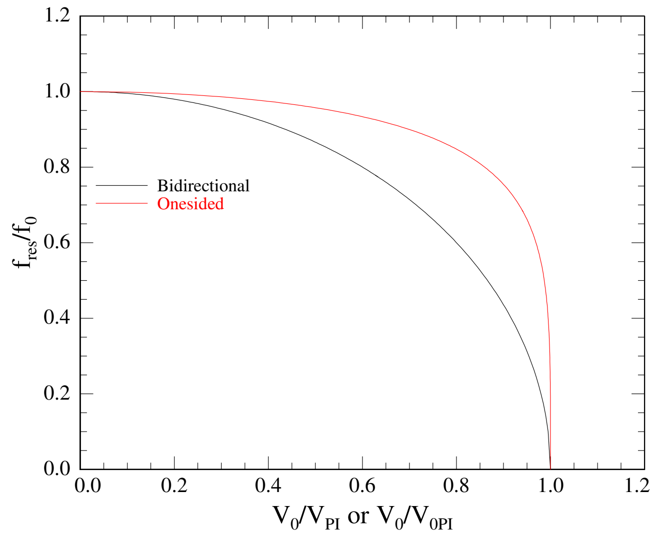

Fig. S5. First order effect of electrostatic spring softening.

5. COMBINING STATIC AND DYNAMIC ACTUATION

In order to linearize a MEMS sweep, it is customary to use a driving signal below the native resonant mechanical frequency. This forced oscillation lies somewhere between DC and the native resonant frequency. Therefore, it is of interest to combine dynamic and static results.

Applying an outer voltage V_0 to fixed electrodes for the bidirectional actuator has implications for static and dynamic MEMS actuation. The pull-in instability voltage can be tuned for static actuation by the applied outer voltage, as shown in Fig. S2. In addition, the static maximum MEMS excursion is affected by the applied outer voltage, reaching its maximum, i.e., $z = \pm z_0/3$, when $V_0 = \sqrt{4/27}V_{0\mathrm{PI}}$. For dynamic actuation, the electrostatic spring softening changes the resonant frequency, shown in Fig. S5, as:

$$f_{\mathrm{res}} = f_0 \times \sqrt{1 - \frac{V_0^2}{V_{0PI}^2}} \tag{S24}$$

where f_{res} is the effective resonant frequency for the native mechanical resonant frequency f_0 with spring softening.

Assuming a maximum voltage constraint on the MEMS, i.e., the right y-axis in Fig. S2, there exists a minimum outer voltage, right x-axis in Fig. S2, in order to make the pull-in on the MEMS equal to the maximum voltage constraint. Assuming the aforementioned, the static and dynamic effects of the outer voltage are depicted in Fig. S6. The figure shows the minimum outer voltage (Min.V_0) normalized to the outer pull-in voltage, normalized maximum displacement, and normalized adjusted resonant frequency as a function of a maximum voltage constraint on the MEMS (Max.V_1) normalized to the outer pull-in voltage. As can be seen, the smaller the maximum voltage constraint, the higher the outer voltage needs to be, which reduces the maximum static MEMS displacement, and in addition, reduces the dynamic resonant frequency. In real applications, one is limited by the output of the electronic waveform generator, i.e., the realistic operating condition for stiff MEMS lies on the left side of the vertical line at Max. $V_1/V_{0\mathrm{PI}} = \sqrt{4/27}$.

6. THE EFFECT OF THE BEAMS IN THE HGC MIRROR

The clamped-clamped beams in the HGC mirror may be rather soft as they have a small cross-section (width $W = 409.5\,\mathrm{nm}$, thickness $h = 400\,\mathrm{nm}$) and are rather long ($L = 10 - 17.74\,\mu\mathrm{m}$). However their resonant frequency is rather high, and thus they do not affect the fundamental mode of the HGC, shown in Fig. S7. The resonant frequency can be found by studying the modes

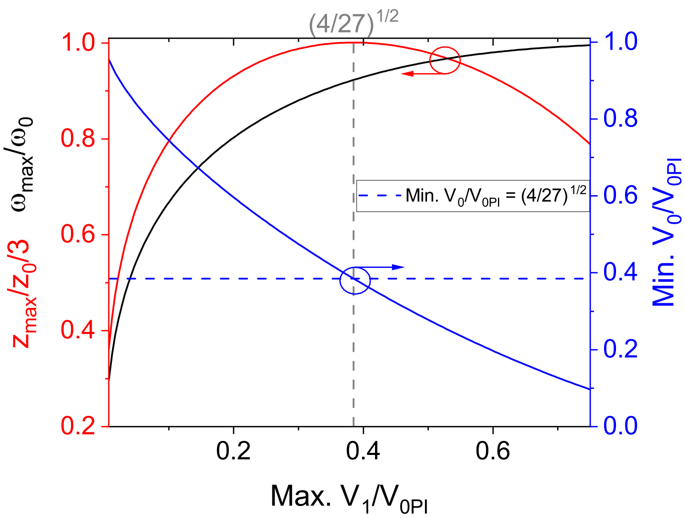

Fig. S6. Normalized maximum displacement and normalized resonant frequency (left) and normalized minimum outer voltage (right) as a function of maximum MEMS voltage Max.V_1 normalized to the outer pull-in voltage. The dashed vertical (horizontal) line shows when the MEMS voltage is equal to the outer voltage, which results in maximum MEMS displacement $z_{max}/z_0/3 = 1$.

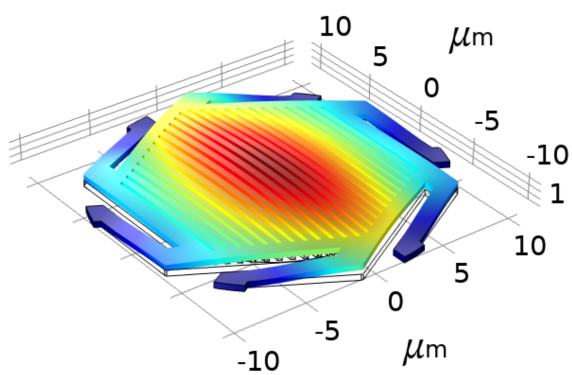

Fig. S7. Mode shape of the fundamental mode of a hexagonal MEMS HCG with an eigenfrequency of 3.79 MHz.

of the dynamic beam equation

$$EIw''''_{xxxx} + \varrho Whw''_{tt} = 0 \Rightarrow \beta_n^4 EIw - \omega_n^2 \varrho Whw = 0,$$

where $E = 170 \times 10^9$ Pa is Young's modulus, $I = \frac{1}{12}Wh^3$ the area moment of inertia, ϱ the mass density, β_n and ω_n are the wavenumber and angular resonant frequency of mode n. This leads to the transcendent characteristic equation for the wavenumber $\cos\beta_n L \cosh\beta_n L = 1$, which for the first mode leads to $\beta_1 L = 4.73$, and thus $\omega_1 = \beta_1^2\sqrt{\frac{EI}{\varrho Wh}} = \beta_1^2\sqrt{\frac{E\frac{1}{12}h^3W}{\varrho Wh}} = \frac{(\beta_1 L)^2}{\sqrt{12}}\frac{h}{L^2}\sqrt{\frac{E}{\varrho}}$ and therefore $f_1 = \frac{(\beta_1 L)^2}{2\pi\sqrt{12}}\frac{h}{L^2}\sqrt{\frac{E}{\varrho}}$, which for the longest beam leads to the resonant frequency $f_1 = \frac{(4.730)^2}{2\pi\sqrt{12}}\frac{400\,\mathrm{nm}}{(17.744\,\mu\mathrm{m})^2}\sqrt{\frac{170\times10^9\,\mathrm{Pa}}{2.33\,\mathrm{g\,cm^{-3}}}} \simeq 11.2\,\mathrm{MHz}$, which is far above the first resonant frequency of the HGC mirror, shown in Fig. S7, thus the flexibility of the beams hardly affects the dynamic behavior of the HGC mirror at the fundamental frequency.

During static deflection the situation is different, as the beams will actually, deflect rather significantly and thus affect the static wavelength tuning. The static deflection w of a clamped-clamped beam under constant load q (force per length) is $w(x) = \frac{q}{24EI}(x - L/2)^2(x + L/2)^2$ which leads to an average deflection $\bar{w} = \frac{qL^4}{24\times30EI} = \frac{qL^4}{24\times30E\frac{1}{12}Wh^3} = \frac{qL^4}{60EWh^3}$, such that the beam has the spring constant of $k_{\mathrm{beam}} = \frac{qL}{\bar{w}} = 60EW\left(\frac{h}{L}\right)^3$.

Thus the longest beam has $k_{\mathrm{beam}} = 60 \times 170 \times 10^9\,\mathrm{Pa} \times 409.5\,\mathrm{nm} \times \left(\frac{400\,\mathrm{nm}}{17.744\mu\mathrm{m}}\right)^3 \simeq 47.9\,\mathrm{N\,m^{-1}}$ which is less than that of the springs for the HGC mirror. However, to estimate the impact of the beams on the total system we have to find the average deflection of all the beams, thus we calculate

$$\langle w\rangle = \frac{\sum_{i=1}^N \bar{w}_i L_i W_i}{\sum_{i=1}^N L_i W_i} = \frac{\sum_{i=1}^N \bar{w}_i L_i}{\sum_{i=1}^N L_i} = \frac{q}{60EWh^3}\frac{\sum_{i=1}^N L_i^5}{\sum_{i=1}^N L_i} = \frac{qL_{\mathrm{eff}}^4}{60EWh^3} \Rightarrow$$

$$L_{\mathrm{eff}} = \sqrt[4]{\frac{\sum_{i=1}^N L_i^5}{\sum_{i=1}^N L_i}} = \sqrt[4]{\frac{1.478\,2\times10^7\mu\mathrm{m}^5}{314.67\mu\mathrm{m}}} = 14.72\,\mu\mathrm{m}.$$

Here L_i is the length, $W_i = W$ the width, and $\bar{w}_i$ the average deflection of the beam i, and $N = 23$ the number of beams. The spring constant corresponding to the effective length $L_{\mathrm{eff}} = 14.72\,\mu\mathrm{m}$ is $k_{\mathrm{eff}} = \frac{qL_{\mathrm{eff}}}{\langle w\rangle} = 60EW\left(\frac{h}{L_{\mathrm{eff}}}\right)^3 = 60 \times 170 \times 10^9\,\mathrm{Pa} \times 409.5\,\mathrm{nm} \times \left(\frac{400\,\mathrm{nm}}{14.72\mu\mathrm{m}}\right)^3 \simeq 84\,\mathrm{N\,m^{-1}}$.

Assuming a spring constant $k_0 = 71\,\mathrm{N\,m^{-1}}$ of the springs for the HGC mirror, we then have the spring constant k_{tot} of the total system

$$k_{\mathrm{tot}} = \left(\frac{1}{k_0} + \frac{1}{k_{\mathrm{eff}}}\right)^{-1} = \left(\frac{1}{71} + \frac{1}{84}\right)^{-1}\mathrm{N\,m^{-1}} \simeq 38.5\,\mathrm{N\,m^{-1}}.$$

Thus the flexibility of the beams affects the static deflection of the HGC mirror significantly.

REFERENCES

1. S. Ramo, J. R. Whinnery, and T. Van Duzer, *Fields and Waves in Communication Electronics* (Wiley, 1965).
2. S. D. Senturia, *Microsystem design* (Kluwer Acad. Publ., 2001).
3. A. V. Lavrinenko, F. Schmidt, N. Gregersen, J. Lægsgaard, and T. Sødergaard, *Numerical methods in photonics* (CRC Press, 2014).
4. Bienstman, Peter, "Rigorous and efficient modelling of wavelength scale photonic components / Peter Bienstman." Ph.D. thesis, Ghent University (2001).
5. Bienstman, Peter and Baets, Roel, "Optical modelling of photonic crystals and VCSELs using eigenmode expansion and perfectly matched layers." Optical and Quantum Electronics **33**, 327–341 (2001).
6. H. K. Sahoo, T. Ansbæk, L. Ottaviano, E. Semenova, F. Zubov, O. Hansen, and K. Yvind, "Tunable mems vcsel on silicon substrate," IEEE J. Sel. Top. Quantum Electron. **25**, 1–7 (2019).

7. P. Qiao, K. T. Cook, K. Li, and C. J. Chang-Hasnain, "Wavelength-swept vcsels," IEEE J. Sel. Top. Quantum Electron. **23**, 1–16 (2017).
8. Keithley, "4200-SCS Semiconductor Characterization System," https://download.tek.com/document/4200SCS_Brochure.pdf.
9. TTi, "AIM-TGF4000," https://resources.aimtti.com/datasheets/AIM-TGF4000_series_data_sheet-Iss1.pdf.
10. Innolume, "FBG-13XX-PM-350," https://www.innolume.com/wp-content/uploads/2021/05/FBG-13XX-PM-350_400.pdf.
11. Haphit, "980/1310/1550/1590nm High Power PM WDM Filter," https://www.haphit.com/pdf/FPWM_980_1550nm_High_Power_PM_WDM_Filter.pdf.
12. Anritsu, "Optical spectrum analyzer MS9740B," https://www.anritsu.com/en-us/test-measurement/products/ms9740b.
13. T. Ansbæk, I.-S. Chung, E. Semenova, O. Hansen, and K. Yvind, "Resonant mems tunable vcsel," I E E E J. on Sel. Top. Quantum Electron. **19**, 1702306 (2013).
14. T. Ansbæk, "Vertical-cavity surface-emitting lasers for medical diagnosis," Ph.D. thesis (2012).